# Magnetic phase diagram of rare-earth orthorhombic perovskite oxides

Alireza Sasani [1], Jorge Iñiguez [2,3] and Eric Bousquet[1]

[1]*Physique Théorique des Matériaux, QMAT, CESAM, Université de Liège, B-4000 Sart-Tilman, Belgium*

[2]*Materials Research and Technology Department, Luxembourg Institute of Science and Technology (LIST), 5 avenue des Hauts-Fourneaux, L-4362, Esch/Alzette, Luxembourg*

[3]*Department of Physics and Materials Science, University of Luxembourg, Rue du Brill 41, L-4422 Belvaux, Luxembourg*

Spin reorientation and magnetization reversal are two important features of the rare-earth orthorhombic perovskites (RMO_3) that have attracted a lot of attention, though their exact microscopic origin has eluded researchers. Here, using density functional theory and classical atomistic spin dynamics we build a general Heisenberg magnetic model that allows to explore the whole phase diagram of the chromite and ferrite compounds and to scrutinize the microscopic mechanism responsible for spin reorientations and magnetization reversals. We show that the occurrence of a magnetization reversal transition depends on the relative strength and sign of two interactions between rare-earth and transition-metal atoms: superexchange and Dzyaloshinskii-Moriya. We also conclude that the presence of a smooth spin reorientation transition between the so-called Γ_4 and the Γ_2 phases through a coexisting region, and the temperature range in which it occurs, depends on subtle balance of metal-metal (superexchange and Dzyaloshinskii-Moriya) and metal–rare-earth (Dzyaloshinsky-Moriya) couplings. In particular, we show that the intermediate coexistence region occurs because the spin sublattices rotate at different rates.

I. INTRODUCTION

Rare-earth orthorhombic perovskites (RMO_3's, where R is an atom of the rare-earth family and M is a transition metal, Fe or Cr in this work) have been studied for a long time due to their unique magnetic properties [1], the two important magnetic behaviors being the spin reorientation (SR) and the magnetization reversal (MR). The SR involves the change of the spin direction from one crystalline direction to another as a function of temperature [see Fig. 1(a)] while MR refers to the inversion of the net magnetization of the crystal as a function of temperature [see Fig. 1(b)]. These materials are also multiferroics (type II, i.e., the magnetic order induces a polarization) [2,3] with strong magnetoelectric (ME) response [2] surpassing most known ME materials. All of these unique properties rely on the presence of two magnetic sublattices R and M with very different Néel temperatures such that for a wide range of temperatures the R spins are paramagnetic while the M spins are ordered. The associated magnetic interactions between these two sublattices have been proved to be the key ingredients for the origin of the SR, MR, and multiferroic properties [4–6], hence for their use in technological applications [7–9]. The SR can happen at high temperatures (480 K in the case of $SmFeO_3$) and this temperature can be lowered by doping which makes it possible to have this behavior at room temperature so that the SR could be used in exchange bias devices [9–12].

Magnetic structures of these materials have been determined from symmetry analysis [13]. In this work we are going to use Bertaut notation for symmetry-adapted magnetic structures, namely, Γ_1, Γ_2, Γ_3, and Γ_4 (see Fig. 2) [14]. Two types of SR are observed, namely, Γ_4 to Γ_2 ($PrFeO_3$, $NdFeO_3$, $SmFeO_3$, $TbFeO_3$, $HoFeO_3$, $ErFeO_3$, $TmFeO_3$, $YbFeO_3$) and Γ_4 to Γ_1 ($CeFeO_3$, $DyFeO_3$) [1].

During the Γ_4 to Γ_2 SR, the spin directions change from the a crystallographic direction to the c direction, slowly rotating as a function of temperature in ac plane. The Γ_4 to Γ_2 SR can develop at different speeds: for some materials it is rather fast (e.g., it spans through a 3-K temperature range [15] for $ErFeO_3$) while for others it can occur over a large temperature range (e.g., 70 K for $NdFeO_3$ [16]). Tsymbal *et al.* have shown that a mean field model can describe the Γ_4 to Γ_2 SR and they observe a sudden jump at the start of the reorientation and a smooth evolution afterwards [15]. Studies on $TbFeO_3$ show that there are two phase transitions, from Γ_4 to Γ_2 below 8.5 K and, then, at the ordering of Tb the Fe subsystem transforms back to Γ_4 [17] which shows the importance of the R site ordering in this SR. It has also been shown that this SR is of second order [18,19] and it could be associated to the softening of a low-frequency magnon mode [20,21]. Bazaliy *et al.* have measured the magnetization of Er in $ErFeO_3$ in the SR region and shown that there is 70% of change [5].

In the Γ_4 to Γ_1 transition, the SR is quite fast and the spins change their directions from a to b crystallographic direction sharply at a well-defined transition temperature. It has been shown that the anisotropic symmetric exchange interactions would be responsible for this SR transition [22].

Several authors built models to describe the magnetic interactions in these materials. Moskvin [23] has made a model to describe the magnetic interactions in $RFeO_3$ and $RCrO_3$
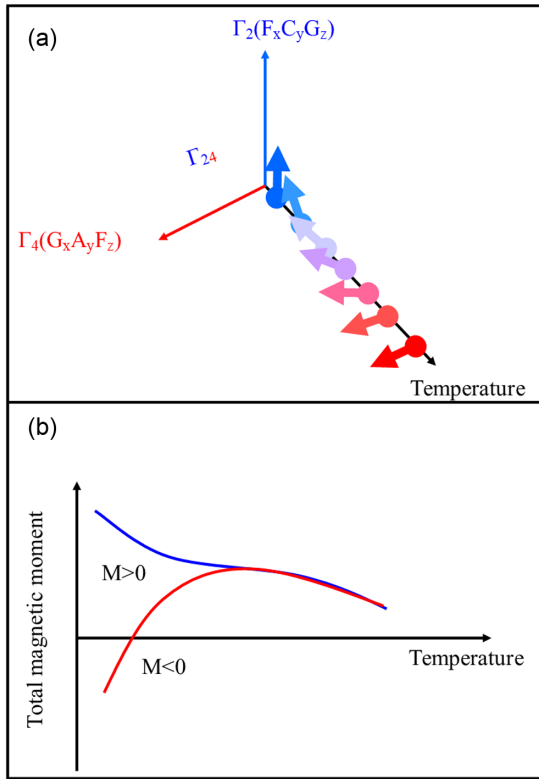
FIG. 1. (a) Schematic representation of the SR from Γ_4 (red color) to Γ_2 (blue color) as a function of temperature where the transition is smooth by passing through an intermediate mixed phase containing both states (Γ_{24}). (b) Schematic plot of the evolution of the total magnetization of the crystal and showing two possible cases: (i) MR effect (red line) where the magnetization changes sign below a critical temperature due to the fact that the paramagnetic rare-earth atom magnetizes in opposite direction to the wFM of the transition-metal atom. (ii) Absence of MR (blue line) where the magnetization is amplified when temperature is reduced and corresponding to the case where the rare-earth atom magnetizes in the same direction as to the wFM of the transition-metal atom.

FIG. 2. (a) Position of transition-metal ions (gray spheres) and rare-earth elements (blue spheres) in *Pnma* structure, purple spheres represent oxygen atoms. (b) Schematic representation of the G, A, C, and F magnetic orders for transition-metal sites present in *Pnma* structure as highlighted by the red box in (a). The arrows represent the positive (red arrows) or negative (purple arrows) value of the magnetic moment. (c) Symmetry-adapted representations Γ_1, Γ_2, Γ_3, and Γ_4 present in perovskites.

and has also made use of Anderson exchange model [24] to study superexchange and Dzyaloshinskii-Moriya interaction (DMI) in these materials [25]. Yamaguchi [6] used a mean field theory model and was more complete than Moskvin. He has shown that some of the SR present in these materials can be explained by antisymmetric and anisotropic symmetric exchange interactions between R and Fe. More recently, Bellaiche *et al.* have given some simple laws to explain the origin of different cantings present in these structures [8]. In their work they have shown that all the cantings on transition-metal sites can be described using simple energy terms originating from the DMI between transition metals. Regarding the interactions between M and R spins, Zhao *et al.* have shown that the DMI between M and R can polarize the R ion and hence could explain the origin of the MR in these materials [7]; according to this work, the MR is linked with a sign in the interaction between the two sublattices that is material dependent and not fully understood.

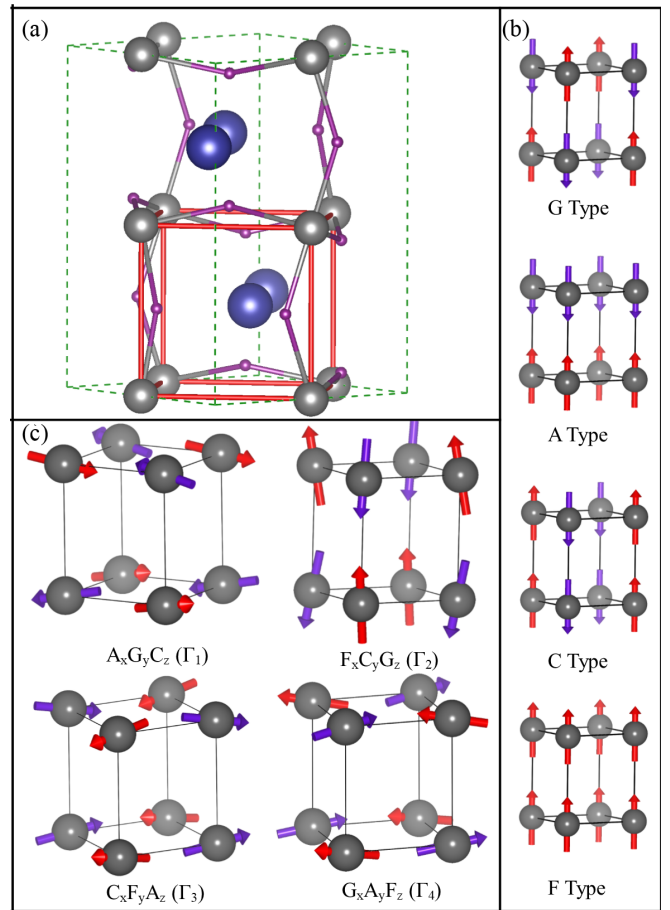Hence, although there has been a great effort to explain the magnetic properties of these materials, a solid and complete understanding regarding SR and MR in these materials and their origin is still missing.

In this paper, we shed some light into the magnetic properties of the RMO$_3$. We have used density functional theory (DFT) to fit a microscopic Heisenberg model that includes the superexchange and the DMI interactions between the magnetic cations M-M and M-R (where M is Cr or Fe, and R is Gd). This model is then used as starting point, and we tune the different parameters to understand their specific role in magnetic behaviors of the material using classical spin dynamics. The spin dynamics results are also compared with analytical solutions to confirm their consistency. Our work allows to explain the origin of the SR and the parameters determining the SR temperature interval and how the R magnetism is affected while in its paramagnetic regime. We find that the occurrence of a slow SR comes from an original evolution of the Γ_4 and Γ_2 orders due to the presence of two different interacting magnetic cations; this allows to have two magnetic phases coexisting while no coupling exists between them in the Hamiltonian.

II. TECHNICAL DETAILS

The main goal of this paper is to give a qualitative picture of the magnetic properties of RMO_3's. We choose to work with Gd because the DFT calculation results are more robust and reliable for fully field f-electron channel (Gd-f^7) that does not have many multiplets. However, the Gd ion is a special case with a very small angular momentum compared to the other rare-earth elements but, once the model is built for Gd, we can tune the model parameter values, i.e., the single-ion anisotropy and DMI, to reproduce the physics of the other rare-earth atoms.

To understand these magnetic behaviors we have used DFT calculations on GdFeO$_3$ and GdCrO$_3$, as reference materials, to have an estimation of the the magnetic interactions in these crystals. We then tuned these parameters to study how they affect the overall magnetic behavior of the system. We build a Heisenberg model containing M-M and M-R superexchange and DMI interactions. Because we will focus on the temperature range where the R sublattice is paramagnetic, we will neglect the R-R interactions (these interactions are nevertheless small as compared to the M-M and M-R couplings). We fit this model against DFT calculations [26,27] done for the orthorhombic *Pnma* phase of GdFeO$_3$ and GdCrO$_3$. We used the VASP package [28,29] and its projected augmented-wave implementation of DFT [30]. We used the so-called PBEsol-GGA [31] functional for the exchange correlation part of the density functional; a Hubbard U correction [32] on Fe, Cr, and Gd of, respectively, 4, 2, and 5 eV has been used with J parameter of 1 and 0.5 eV on Fe and Cr. All the calculations were done with a $6 \times 6 \times 4$ mesh of k points for sampling the reciprocal space and a cutoff energy on the plane-wave expansion of 700 eV to have a good convergence on single-ion anisotropic and DMIs (less than 5 μeV convergence).

The calculations of the superexchange interactions were done using the Green's function method as implemented in the TB2J [33] code. In this method the maximally localized Wannier function [34] as implemented in WANNIER90 [35] are calculated using DFT (VASP interface to maximally localized Wannier functions) and using these Wannier functions and the Green's function method, the superexchange parameters are calculated. Some of these superexchange interactions were compared to the ones calculated using total energy to ensure the consistency of the method. To calculate the DMI couplings, we calculated the energy of different spin configurations and used the method given by Xiang *et al.* [36]. We have checked that the results are qualitatively the same by using different Hubbard U and J corrections while we have used the ones giving the best Néel temperature for both sublattices. All of the fitted magnetic interaction parameters were used to do spin dynamics with the VAMPIRE code [37]. In this code the Landau-Lifshitz-Gilbert (LLG) equation for the spin dynamics [Eq. (1)] is solved numerically:

$$\frac{\partial S_i}{\partial t} = \frac{\gamma}{1+\lambda^2}\big[S_i \times B_{\text{eff}}^i + \lambda S_i \times \big(S_i \times B_{\text{eff}}^i\big)\big]. \quad (1)$$

In the temperature-dependent spin dynamics simulations we have used a simulation cell of 20 nanometers in each direction. The thermalization step was done in 50 000 time steps of

TABLE I. Irreducible representation of magnetic states present in the *Pnma* phase of RMO_3 for both transition-metal M site and R site [14].

Irrep	M site	R site
Γ_1	$(A_x, \bar{G}_y, C_z)$	$(0,0,C_z)$
Γ_2	$(F_x, C_y, \bar{G}_z)$	$(F_x, C_y, 0)$
Γ_3	$(\bar{C}_x, F_y, A_z)$	$(C_x, F_y, 0)$
Γ_4	$(\bar{G}_x, A_y, F_z)$	$(0,0,F_z)$

1.5 fs and the measurement is done in 90 000 time steps of 1.5 fs.

Before analyzing the fitted model, we start with an analytical model of the magnetic interactions present in RMO_3 systems.

III. ANALYTICAL MODEL

To understand the mechanism behind SR and MR, we develop in this section the Heisenberg model and solve it analytically to understand the phase diagram of RMO_3 versus their microscopic magnetic interactions. This will also allow to compare with the spin dynamics calculations to confirm that both give consistent results.

A. Symmetry-adapted spin representation

We develop an analytical model of RMO_3 using the symmetry-adapted spin representation. For each of the sublattices (M or R) in the *Pnma* unit cell, we have four magnetic sites that result in four different magnetic orders: A, C, G, and F type as presented in Fig. 2(b). Using these four magnetic orderings, we can define four symmetry-adapted spin states, namely, Γ_1, Γ_2, Γ_3, Γ_4 that are linear combination of the A, G, C, and F orderings in different directions (Fig. 2) [14]. Because the ground state of the M spin sublattice is a robust G-type antiferromagnetic ordering in the *Pnma* perovskite phase, the most relevant Γ_j states are those with $j = 1$, 2, and 4, which present a dominant G type in one of the three crystallographic directions with the presence of canted A-, C-, and F-type magnetic orders in the other directions. We summarize in Table I the different Γ_j states where $\bar{G}$ shows the main magnetic order and the components without a bar are small spin cantings.

Using these notations, we can write the symmetry-adapted magnetic states in terms of their modulation vectors for magnetic sublattice a as follows [Eq. (2) to Eq. (5)]:

$$S_{i,a}^{\Gamma_1} = A_{a,x}(-1)^{(n_z^i)} + \bar{G}_{a,y}(-1)^{(n_x^i+n_y^i+n_z^i)} + C_{a,z}(-1)^{(n_x^i+n_y^i)}, \quad (2)$$

$$S_{i,a}^{\Gamma_2} = F_{a,x} + C_{a,y}(-1)^{(n_x^i+n_z^i)} + \bar{G}_{a,z}(-1)^{(n_x^i+n_y^i+n_z^i)}, \quad (3)$$

$$S_{i,a}^{\Gamma_3} = C_{a,x}(-1)^{(n_y^i+n_z^i)} + F_{a,y} + A_{a,z}(-1)^{(n_z^i)}, \quad (4)$$

$$S_{i,a}^{\Gamma_4} = \bar{G}_{a,x}(-1)^{(n_x^i+n_y^i+n_z^i)} + A_{a,y}(-1)^{(n_z^i)} + F_{a,z}. \quad (5)$$

Here $S_{i,a}^{\Gamma_j}$ is the spin of lattice site i for magnetic sublattice a (M or R) in irreducible representation Γ_j and the lattice site

vector for lattice site i can be written as $n_x^i \hat{u}_1 + n_y^i \hat{u}_2 + n_z^i \hat{u}_3$ where $\hat{u}_1$, $\hat{u}_2$, and $\hat{u}_3$ are unit-cell vectors while the coefficients G, A, F, and C represent the magnitude of spin canting in each direction, the G-type order being the main one. From now on, we will use these spin representations in our Heisenberg model.

B. Heisenberg model

In this section, we develop the Heisenberg Hamiltonian for RMO_3 in which we include the magnetic interactions between all the magnetic species: transition-metal atoms (M) and rare-earth atoms (R), which can be summarized as follows if one stays at the second order of interactions (higher-order spin interactions like biquadratic or four-spin couplings are neglected):

$$H = H^{MM} + H^{RM} + H^{RR}, \tag{6}$$

where H^{MM} is the Hamiltonian of M-M interactions, H^{RR} the Hamiltonian of R-R interactions, and H^{RM} the Hamiltonian of R-M interactions. H^{MM} can be written as follows:

$$H^{MM} = H_{ex}^{MM} + H_{DMI}^{MM} + H_{SIA}^{MM}, \tag{7}$$

where H_{ex}^{MM}, H_{DMI}^{MM}, and H_{SIA}^{MM} represent the superexchange, DMI, and single-ion anisotropy (SIA) interactions of the M cations. In our simulations we have neglected anisotropic symmetric exchange interactions since our DFT calculations show that they are two orders of magnitude smaller than DMIs (results not shown here).

For H^{RR} we have neglected the H_{ex}^{RR} and H_{DMI}^{RR} since we are interested in behaviors that take place at temperatures higher than the Néel temperature of the R spin sublattice. We will only keep the SIA interactions for this site:

$$H^{RR} = H_{SIA}^{RR}. \tag{8}$$

The Hamiltonian taking care of the R-M interactions can be written as follows:

$$H^{RM} = H_{ex}^{RM} + H_{DMI}^{RM}. \tag{9}$$

The superexchange, DMI, and SIA terms can be developed as follows:

$$H_{ex}^{ab} = \frac{1}{2} \sum_{ij}^{N} (J_{ab,ij} S_{i,a} . S_{j,b}), \tag{10}$$

$$H_{DMI}^{ab} = \frac{1}{2} \sum_{i,j} (D_{ab,ij} \times S_{j,a}) \cdot S_{i,b}, \tag{11}$$

$$H_{SIA}^{aa} = \sum_{i} K_a (S_{i,a} \cdot \hat{e}_i)^2, \tag{12}$$

where ab could be $a = b = M$, $a = b = R$ or $a = M$ and $b = R$, and $\hat{e}_i$ is a unit vector pointing to the direction of the SIA axis, which, according to our DFT calculation for $GdFeO_3$ and $GdCrO_3$, is the easy axis.

We can show that there is no interaction between the different Γ_j magnetic orderings [see Supplemental Material (SM) [38]] such that we can write the total energy of the system as the sum of the energy of each state. In this case we can write the total energy as

$$H = H^{\Gamma_1} + H^{\Gamma_2} + H^{\Gamma_3} + H^{\Gamma_4}. \tag{13}$$

In our analytical derivations we have neglected the Γ_3 state since this state is much higher in energy than Γ_1, Γ_2, and Γ_4. This is related to the fact that the Γ_3 state does not contain G-type order, which is the order driving the lowest energy in the crystal through the strongest superexchange interactions between transition metals.

By putting the spin states in the Hamiltonian we can derive the following expressions for each of the states (see SM [38]):

$$
\begin{aligned}
H^{\Gamma_1} &= H_{ex}^M + H_{DMI}^M + H_{ex}^{RM} + H_{DMI}^{RM} \\
&= NJ^M(A_{M,x})^2 - 3NJ^M(\bar{G}_{M,y})^2 - NJ^M(C_{M,z})^2 - 6Nd_x^M \bar{G}_{M,y} C_{M,z} - 6Nd_y^M C_{M,z} A_{M,x} - 6Nd_z^M A_{M,x} \bar{G}_{M,y} \\
&\quad - 8Nd_x^{RM} C_{R,z} \bar{G}_{M,y} - 8Nd_y^{RM} C_{R,z} A_{M,x},
\end{aligned} \tag{14}
$$

$$
\begin{aligned}
H^{\Gamma_2} &= H_{ex}^M + H_{DMI}^M + H_{ex}^{RM} + H_{DMI}^{RM} \\
&= 3NJ^M(F_{M,x})^2 - NJ^M(C_{M,y})^2 - 3NJ^M(\bar{G}_{M,z})^2 - 6Nd_x^M C_{M,y} \bar{G}_{M,z} - 6Nd_y^M \bar{G}_{M,z} F_{M,x} - 6Nd_z^M F_{M,x} C_{M,y} \\
&\quad - 8NJ^{RM} F_{M,x} F_{R,x} - 8Nd_x^{RM} \bar{G}_{M,z} C_{R,y} - 8Nd_y^{RM} F_{R,x} \bar{G}_{M,z} - 8Nd_z^{RM} F_{R,x} C_{M,y} - 8Nd_z^{RM} C_{R,y} F_{M,x},
\end{aligned} \tag{15}
$$

$$
\begin{aligned}
H^{\Gamma_4} &= H_{ex}^M + H_{DMI}^M + H_{ex}^{RM} + H_{DMI}^{RM} + H_{SIA}^R + H_{SIA}^M \\
&= -3NJ^M(\bar{G}_{M,x})^2 + NJ^M(A_{M,y})^2 + 3NJ^M(F_{M,z})^2 - 6Nd_x^M A_{M,y} F_{M,z} - 6Nd_y^M \bar{G}_{M,x} F_{M,z} - 6Nd_z^M \bar{G}_{M,x} A_{M,y} \\
&\quad - 8NJ^{RM} F_{M,z} F_{R,z} - 8Nd_x^{RM} F_{z,R} A_{M,y} - 8Nd_y^{RM} F_{R,z} \bar{G}_{M,x} - NK^M(\bar{G}_{M,x})^2 - NK^R(\bar{G}_{R,x})^2,
\end{aligned} \tag{16}
$$

where J^M and J^{RM} are, respectively, the superexchange interaction magnitude for M sublattice and between R and M spins (J^a is considered as J_{ii} for isotropic exchange interaction); d_i^a is the magnitude of ith component of DMI vector for magnetic sublattice a; and N is the number of magnetic

atoms, while K^a represent the SIA magnitude of magnetic sublattice a.

With Eqs. (14)–(16) we have decomposed the Hamiltonian in terms of three independent representations Γ_1, Γ_2, and Γ_4, themselves decomposed into the superexchange, DMI,

TABLE II. Calculated magnetic interactions from DFT of $GdFeO_3$ and $GdCrO_3$. J (average values between nearest neighbors) values are for the nearest neighbors and d_i are the DMI vector components along $i = x$, y, and z. The units are meV multiplied by the spin moment multiplication shown in the last column, which is convenient for comparing different systems with different spin amplitudes. To get the values in meV, the reported magnetic interactions should be divided by the spin multiplication values reported in the last column.

	d_x	d_y	d_z	J	$S_1 S_2$
Fe-Fe	0.000	-1.805	-1.104	38	$\frac{25}{4}$
Cr-Cr	-0.001	-0.810	-0.600	7.2	$\frac{9}{4}$
Gd-Fe	0.008	-0.064	0.031	1.85	$\frac{35}{4}$
Gd-Cr	-0.010	0.042	-0.019	2.15	$\frac{21}{4}$
Gd-Gd				0.19	$\frac{49}{4}$

and SIA of their constituent A, C, G, and F magnetic orderings. This form allows us to decompose the different microscopic contributions of the magnetic energy of the RMO_3 systems.

IV. DFT CALCULATION OF THE MAGNETIC INTERACTION PARAMETERS

In this section we will present the parameters that we have calculated using DFT for $GdFeO_3$ and $GdCrO_3$, which will serve as a reference starting point in our spin dynamics simulations. These values will guide us to scan the magnetic phase diagram in regions that are relevant for these materials.

A. Superexchange and DMI parameters

The dominant interactions are the superexchange interaction between transition metals. The DFT results for $GdFeO_3$ and $GdCrO_3$ show that the strongest superexchange interactions are between the nearest-neighbor transition metals; going further in distance gives very small values with respect to the nearest neighbors such that they can be neglected. These interactions are 38 and 7.2 meV for nearest neighbors (see Table II), in $GdFeO_3$ and $GdCrO_3$, respectively, and 1 meV or below for the next-nearest neighbors. The R-M superexchange interactions are one order of magnitude smaller (approximately 2 meV) than the ones between transition metals. The R-R superexchange interactions are two orders of magnitude smaller than the transition-metal ones (around 0.2 meV) such that we have neglected the R-R interactions in our spin dynamics simulations. Calculated SIA for both sublattices in $GdFeO_3$ shows that these parameters are small around 72 μeV for Gd with easy axis along c direction and 75 μeV for Fe with easy axis along the b in the $Pnma$ structure; in $GdCrO_3$ the SIA constant for Cr in along c direction and it is 25 μeV.

The most relevant parameters for our behaviors of interest are the DMIs. Table II shows the obtained results, where the relation $d_y > d_z \gg d_x$ always holds. It is the $\bar{a}\bar{a}\bar{c}^+$ octahedral rotation pattern that breaks the bond inversion center of symmetry and creates the DMI [39]. Hence, we will have the biggest distortion in the [110] cubic direction (amplitude of the rotations in the y direction of the $Pnma$ structure) and the
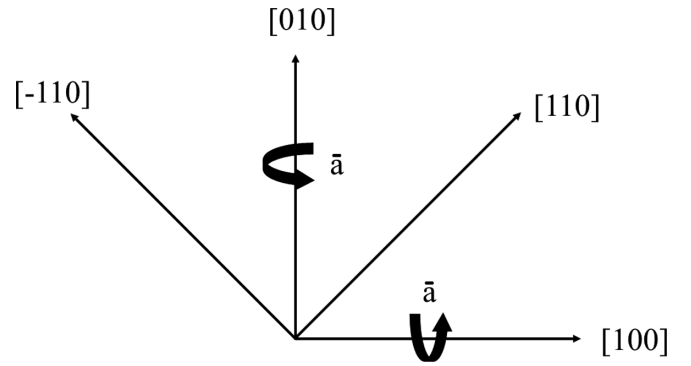

FIG. 3. Schematic presentation of the cubic ([100] and [010]) and $Pnma$ ([110] and [$\bar{1}$10]) crystallographic directions with respect to each other. The curved arrows represent the oxygen octahedra rotations that are in the same direction when projected in the [110] direction while they are in opposite direction when projected in the [$\bar{1}$10] direction.

smallest one will be in the [$\bar{1}$10] cubic direction (x direction of the $Pnma$ structure) (as shown in Fig. 3 the oxygen octahedral rotation has the same sign in the [110] direction and add up while in the [$\bar{1}$10] direction they have opposite sign and subtract from each other), while the distortion in the [001] cubic direction (c direction of $Pnma$) will be almost half of the one in the [110] cubic direction. The ratio between these distortions is close to be the same for any $Pnma$ crystal and this structural ratio also drives the key magnetic interactions as we will show below.

At high temperatures there is no magnetic ordering on R sites (paramagnetic phase) and the interactions between the R spins are negligible. Hence, at high temperatures the SIA and DMI interactions of the M sites determine the magnetic equilibrium state. From the formulas (14)–(16) we can notice that both d_y^M and d_z^M, which have the biggest components compared to d_x^M (see Table II) in the Γ_4 state, are coupled with the main magnetic order and spin direction (i.e., $G_{M,x}$), making the energy of this state lower compared to Γ_1 and Γ_2. When comparing Γ_1 and Γ_2, we can observe that for the Γ_2 state we have the d_y^M terms that couple with the main spin direction, hence stronger than the d_z^M component present in Γ_1. This implies that the Γ_2 state is lower in energy than the Γ_1 state. Hence, we can have $E_{\mathrm{DMI}}^{MM,\Gamma_4} < E_{\mathrm{DMI}}^{MM,\Gamma_2} < E_{\mathrm{DMI}}^{MM,\Gamma_1}$, where $E_{\mathrm{DMI}}^{MM,\Gamma_j}$ is the energy from DMI between M atoms in the Γ_j state, i.e., the DMI between M cations favor the Γ_4 state [23].

We can also see the effect of these interactions in $RCrO_3$ structures. According to Table II the DMIs and superexchanges in these structures are smaller than for $RFeO_3$, which makes the energy difference between different spin orders (Γ_1, Γ_2, Γ_4) smaller. This is consistent with the fact that the Γ_2 and Γ_4 states are both present at high temperature for the $RCrO_3$ crystal series [40].

Considering the DMIs between R and M, we notice that in the Γ_2 state we have $H_{\mathrm{DMI}}^{RM,\Gamma_2} = -8Nd_x^{RM}\bar{G}_{M,z}C_{R,y} - 8Nd_y^{RM}F_{R,x}\bar{G}_{M,z} - 8Nd_z^{RM}F_{R,x}C_{M,y} - 8Nd_z^{RM}C_{R,y}F_{M,x}$ terms in which d_y^{RM} couples with the main spin directions and also this state has more degrees of freedom compared to the

other states making energy of this state lower. As for Γ_4 we have $H_{\text{DMI}}^{RM,\Gamma_4} = -8Nd_x^{RM}F_{z,R}A_{M,y} - 8Nd_y^{RM}F_{R,z}\bar{G}_{M,x}$ and for Γ_1 we have $H_{\text{DMI}}^{RM,\Gamma_1} = -8Nd_x^{RM}C_{R,z}\bar{G}_{M,y} - 8Nd_y^{RM}C_{R,z}A_{M,x}$ which again due to having the coupling $8Nd_y^{RM}F_{R,z}\bar{G}_{M,x}$ compared to $8Nd_x^{RM}C_{R,z}\bar{G}_{M,y}$ terms the Γ_4 state is lower than that of Γ_1 ($d_y^{RM} \gg d_x^{RM}$). Hence, we can write the order of the different energies due to DMI of R and M as $E_{\text{DMI}}^{RM,\Gamma_2} < E_{\text{DMI}}^{RM,\Gamma_4} < E_{\text{DMI}}^{RM,\Gamma_1}$.

From this analysis, we can see why a SR transition is possible when lowering the temperature.

Indeed, as the temperature is lowered, the interactions between R and M cations become stronger due to the magnetization of the R site in the field created by the M spins, and the Γ_2 is more and more favored through the DMIs between R and M sites. Hence, we can explain the Γ_4 to Γ_2 SR due to the DMIs between R and M sites as discussed previously by Yamaguchi [6].

B. Origin of ordering on R site

The MR observed in $RM\text{O}_3$ is the change of sign in the net magnetization of the material. This property has been related to the polarization of the R site atoms as a result of interaction with transition-metal atoms. In this interaction R site atoms could polarize in the direction of the weak magnetic moment of the transition metal or in opposite direction, which would result in the presence or the absence of the magnetization reversal respectively [see Fig. 1(b)]. The remaining question is why the R paramagnetic atoms magnetize in the opposite direction for some R elements (e.g., NdFeO$_3$, SmFeO$_3$, DyFeO$_3$, ErFeO$_3$, TmFeO$_3$, YbFeO$_3$) and why they magnetize in the same direction for others (e.g., PrFeO$_3$, EuFeO$_3$, GdFeO$_3$, TbFeO$_3$, HoFeO$_3$) [41] and what is the microscopic origin of this effect.

With our model we can have access to the detailed microscopic interaction between R and M cations. Equations (14)–(16) show that there are two types of interactions acting on R sites: (i) the superexchange interaction between the weak ferromagnetic (wFM) order of the M and R sublattices ($J_{RM}F_MF_R$) and (ii) the DMI between the G-type orders on the M and R sublattices ($d_y^{RM}F_{R,(z,x)}\bar{G}_{M,(x,z)}$ and $d_x^{RM}C_{R,z}\bar{G}_{M,y}$). These interactions can induce either F- or C-type ordering on R site. To check the validity of these possibilities, we have used DFT calculations as computer experiments where we have replaced the R site by Cr in GdFeO$_3$'s *Pnma* structure to allow the study of full noncollinear calculations and to have stronger RM site interactions compared to the Gd case. Our model is valid for two magnetic sublattices in perovskites whatever the magnetic cations, such that replacing R by Cr will show the same qualitative trend.

We have done different calculations in which we constrained the magnetic moments on the Fe site and relaxed the magnetic order of the R site within two different settings. In the first setting, we set the spin-orbit coupling (SOC) to zero to suppress the DMI such that the resulting magnetic order on R site would be due to superexchange interactions only. In the second setting, we considered SOC, hence activating the second term ($d_y^{RM}F_{R,(z,x)}\bar{G}_{M,(x,z)}$) that couples the G-type order of the M sublattice to F order on R site. In Fig. 4 we show the
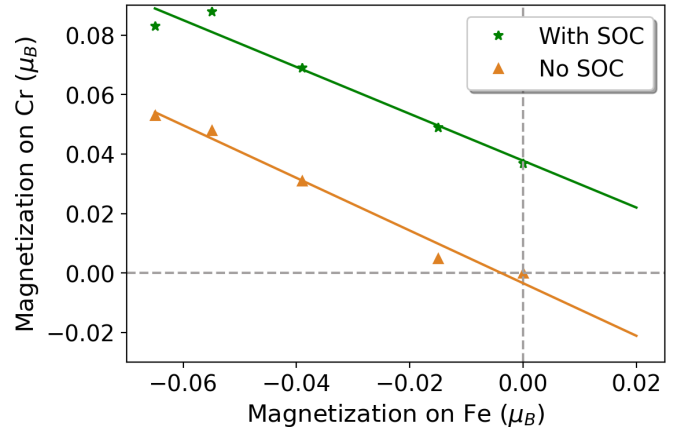

FIG. 4. Calculated magnetization of Cr as a function of magnetization of Fe in CrFeO$_3$ simulated at fixed atomic positions of relaxed *Pnma* GdFeO$_3$ (Gd is replaced by Cr). Orange points are without spin-orbit coupling (with a linear fit orange line) and green points are with spin-orbit coupling (with linear fit green line).

result of these two types of calculations where we can see that the magnetization line jumps to higher values when the SOC is present. This shows that the DMI can polarize the R site as the superexchange, which is in agreement with the results obtained by Zhao *et al.* [7] using DMI energetic expressions between R and M sites.

We should also mention that in our simulations for $R = \text{Cr}$, since the superexchange interaction is AFM, it polarizes the R site in the opposite direction to the wFM direction of the M, while the DMI polarizes the R site in the same direction as the wFM of the M site (see Fig. 4). Our calculations for GdFeO$_3$ also show that these interactions are in competition with each other such that the final magnetization direction of the R site will be determined by the balance between them.

Considering GdCrO$_3$ we can see in Table II that the DMI interactions between the Gd and Cr spins have opposite sign compared to the DMI interaction between Gd and Fe spins. This shows that we can also have the sign change of the DMI depending on the electronic structure of the atoms in the structure. In this case both the DMI and superexchange induce a polarization in the same direction and, indeed, the calculated magnetic ground state of the GdCrO$_3$ shows that the wFM of Cr and polarization of the Gd are in opposite directions, while for GdFeO$_3$ the wFM of the iron atoms and the polarization direction of the Gd atoms are in the same direction. Hence, depending on the electronic structure of the atoms we can have the superexchange and DMI that compete or cooperate that will result in the presence or the absence of the MR. This shows that the DMI between the two sublattices is the interaction that is responsible for polarizing the R site. The calculated DMI interaction signs are in agreement with experimental results which show that for GdFeO3 there is no MR [41] while it is present in GdCrO3 [42,43].

V. SPIN DYNAMICS

In this section we present the spin dynamics results obtained with the VAMPIRE code through the Heisenberg model
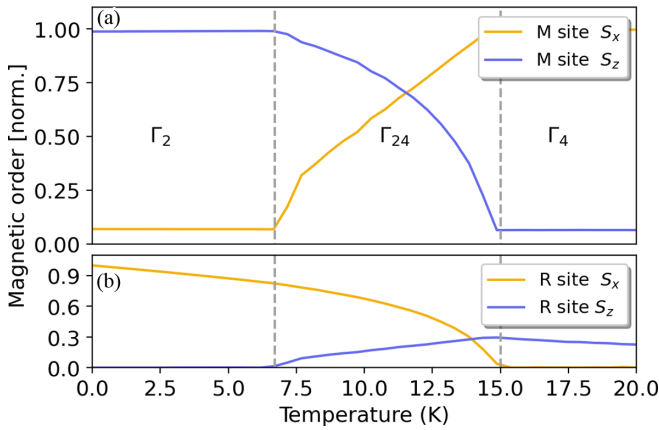
FIG. 5. Temperature-dependent SR as obtained from our spin dynamics calculations. (a) Shows the transition-metal M site spin projections along the x and z directions. (b) Shows the evolution of the x and z magnetic moment projection of the rare-earth R site in the same temperature range as (a). The units on the y axis are spins normalized with their moments ($\frac{5}{2}$ and $\frac{7}{2}$ for Fe and Gd, respectively).

FIG. 6. Temperature-dependent spin dynamics results for $GdFeO_3$: (a) normalized magnetic moment of the Fe site as projected along z and x directions (F_z and G_x) and (b) normalized magnetic moment of the Gd site (ferromagnetic order along the z direction). We also show the fit of the magnetic order of Fe sublattice against $(1 - \frac{T}{T_N})^\beta$ as represented by the green dashed line.

presented above (with R-R superexchange and DMI set to zero). First, we worked with the magnetic interaction parameters obtained for $GdFeO_3$. Then, we made additional spin dynamics calculations by varying the values of these parameters (related to larger spin-orbit interaction present in other rare-earth elements) to understand how the phase diagram and associated SR transitions are affected by the change of the magnetic interactions.

To verify that our model qualitatively respects the symmetry of the *Pnma* phase of RMO_3 compounds, we first simulated the ground state (0 K) of these structures by tuning the SIA to obtain the magnetic moment direction along the different x, y, and z crystallographic directions. By doing so, we verified that the obtained cantings actually correspond to the ones of the Γ_4, Γ_1, and Γ_2 orders when magnetic moments lie along x, y, and z directions, respectively (see Table I).

In the following we will analyze both Γ_4 to Γ_2 and Γ_4 to Γ_1 SR transitions.

A. Γ_4 to Γ_2 reorientation

As a first step we have done temperature-dependent SR. To have temperature-dependent SR, we have tuned the parameters obtained for $GdFeO_3$ so as to induce such behavior since this effect is not present in $GdFeO_3$. More precisely, we increase the DMI interaction between R and M by one order of magnitude to have the SR. Figure 5(a) shows the evolution of the magnetic moment directions with respect to the temperature when there is a SR, as obtained from our spin dynamics simulations.

We can see a slow rotation of the spins from x to z direction as the temperature decreases and that this reorientation is continuous in a range of temperature where the two orders (associated to the Γ_4 and Γ_2 states) are present together. Figure 5(b) shows the temperature evolution of the magnetic ordering of the R spins due to its interaction with the M spins. Here, we can see that the SR happens around 15 K when the normalized magnetic moment of the rare-earth element is
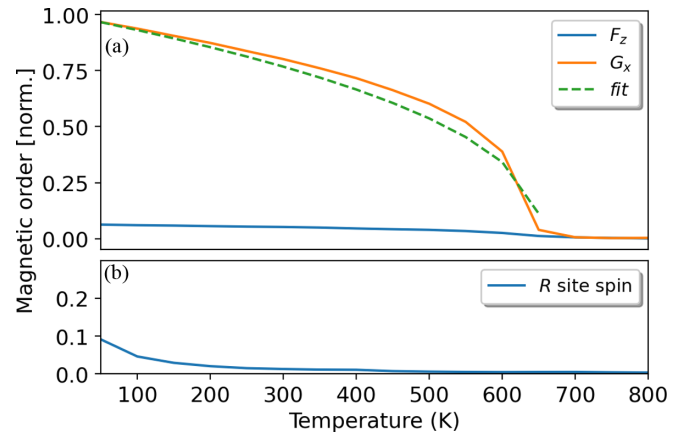
about 0.3. Below this critical temperature, the R site magnetic moment increases in a more pronounced way. The magnetization of the R sites creates a torque that induces the rotation of the M magnetic direction. Such an increase of the ferromagnetic moment of the R site has been observed experimentally for $ErFeO_3$ in the SR region [5]. This result shows that we need the ferromagnetic ordering on the R site to have this Γ_4 to Γ_2 SR transition. This is also observed experimentally in, e.g., $TbFeO_3$ where the crystal goes from the Γ_2 state to the Γ_4 state when the Tb atom orders into the $A_x G_y$ magnetic phase (no ferromagnetic order) at very low temperatures [17].

In Fig. 6(a) we report the evolution of the magnetic orders at higher temperature. We obtain from it a Néel temperature of 654 K (using the M-M superexchange parameters as obtained for $GdFeO_3$) which is calculated by fitting the curve with $(1 - \frac{T}{T_N})^\beta$ with $\beta = 0.44$ (green dashed line). The wFM (F_z) appears at temperatures below the Néel temperature and, after a jump at the phase transition, stays constant ($0.10 \times \frac{5}{2} \mu_B$). In Fig. 6(b) we show the evolution of the R site magnetic moments where we can see that the induced magnetization of the rare-earth spins is visible at temperatures as high as 400 K.

To further understand the SR, we have studied how the stability of the magnetic orders is affected by the value of the DMI coupling between R and M. This allows us to determine how the strength of the interaction between R and M spins influences the SR. Figure 7 shows the equilibrium state of the structure which is projected to the different irreducible magnetic orders along x, y, and z directions versus d_z^{RM}. (The figure presents three components of the spin as projected to different irreducible representations.)

For values of $d_z^{RM} < 1.6$ (meV) we can see that we have the Γ_4 state with the main direction of the spin along x with G-type AFM order (G_x) and small components (canting) of the spins along the y and z directions with A-AFM (A_y) and FM (F_z) ordering, respectively. For 4.3 (meV) $> d_z^{RM} >$ 1.6 (meV) we have a coexisting region that we denote Γ_{24}, where mostly Γ_2 and Γ_4 states are present. The system enters
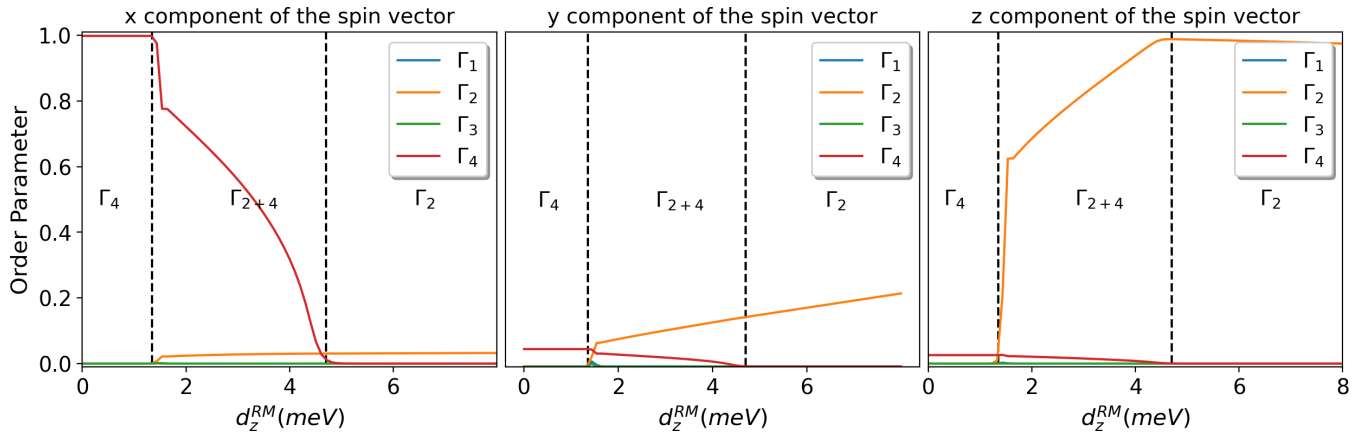
FIG. 7. Decomposition of magnetic ordering on different irreducible representations (Γ_j) for x, y, and z directions of the spins in the Γ_4 to Γ_2 SR phase transition case. The calculations are done at 0 K (ground state). The horizontal axis shows the magnitude of the z component DMI between R and M sites in the units of meV times the multiplication of the spin amplitudes (see Table II) and the vertical axis shows the normalized order-parameter magnitude.

to this state through a sudden jump in magnetic order (we also have a discontinuity in the energy of the system). As we move towards higher values of d_z^{RM} the Γ_4 contribution is reduced while Γ_2 contribution increases up to $d_z^{RM} > 4.3$ (meV) where only the Γ_2 is present, the SR being completed. The transition from $\Gamma_2 + \Gamma_4$ to Γ_2 at $d_z^{RM} = 4.3$ (meV) is continuous.

To get further insight into this transition, in Fig. 8 we show the evolution of the atomic site projection of the spins in x, y, and z components. Since the SR transition is due to the $d_z^{RM} F_{R,x} C_{M,y}$ term in the Hamiltonian, we can observe an increase of the C-type canted order along the y direction as the interaction between R and M becomes stronger. Additionally, since the magnitude of the canted ferromagnetic order on M is constant (FM order along the x and z directions before and after SR), this increase in C-type order can only come from a reduction of the G-type order component of the spin.

In Fig. 9 we show how the different energy contributions of the system (superexchange and DMI) evolve with respect to the d_z^{RM} parameter. We can see that the contributions coming from d_z^M and superexchange interactions between transition metals are positive and increase as we go from Γ_4 to Γ_2 state, which means that they are against the SR. In fact, these interactions are determinant for how fast the SR happens. The superexchange interaction is the main interaction that resists against the SR and this is due to the fact that the SR involves an increase of the C-type ordering on M sites (via $d_z^{RM} F_{R,x} C_{M,y}$, as mentioned above) and the reduction of the G-type order, which costs some energy. Therefore, to overcome this energy penalty we need larger interaction between R and M to complete the SR which is provided by more ordering of the R site atoms.

1. Parameters affecting the Γ_4 to Γ_2 SR

One of the properties that is important to understand is the temperature range in which the spins start and complete their reorientation. From our model, we found that three parameters affect how fast the SR happens: the DMI d_z^{RM} between R and M cations (related to the ordering amplitude of the

R sites), the DMI d_z^M between M cations, and the superexchange interaction $J^{\tilde{M}}$ between M cations. The ratios between these three parameters drive and determine the energy difference between the Γ_4 and Γ_2 states and hence the temperature range where the SR takes place.

To highlight these parameter effects we report in Figs. 10 and 11 a two-dimensional (2D) plot showing the presence of the Γ_4, Γ_2, and Γ_{24} regions with respect to $d_z^{\tilde{M}}$ and d_z^{RM} values at fixed J^M as calculated for GdFeO$_3$. Figure 11 shows the same but for a fixed value of J^M corresponding to the one calculated for GdCrO$_3$. As we can see, for too small values of d_z^M the system only experiences an abrupt transition (first order) between Γ_4 and Γ_2 without any coexisting region and the ratio between d_z^M and d_z^{RM} at which the transition appears is rather constant. However, beyond a critical value of d_z^M a Γ_{24} coexisting region appears and grows with the amplitude of d_z^M. This means that, for a given value of J^M, if d_z^M is not large enough the system will never experience a slow SR. Once the coexistence region opens, it grows very fast with d^M such that for large enough d_z^M and d_z^{RM} values a slow SR transition is always guaranteed. On the other side, in Figs. 10(b) and 11 we can see how the coexisting region area is affected by the value of J^M at a fixed value of d_z^M. Here we can remark that if J^M is too large or too small, then the Γ_{24} area is strongly reduced.

In Figs. 10 and 11 we also draw the maximum and minimum values of d_z^M and J^M as obtained for RFeO$_3$ and RCrO$_3$, respectively, for the whole series of lanthanides $R = $ La to Lu (horizontal dashed lines). We can see that the range of these parameters is not too large and that they cross small areas of the coexistence region where SR is possible. We can remark that the SR area for $M = $ Cr is particularly small while it is potentially larger for Fe.

These phase diagrams help if one wants to design engineering of SR speed in these crystals. For example, if a slower SR is desired, the Fe case will be more interesting through doping with atoms that will reduce the superexchange interactions between irons and/or that will increase the DMI between irons (increase of the wFM).
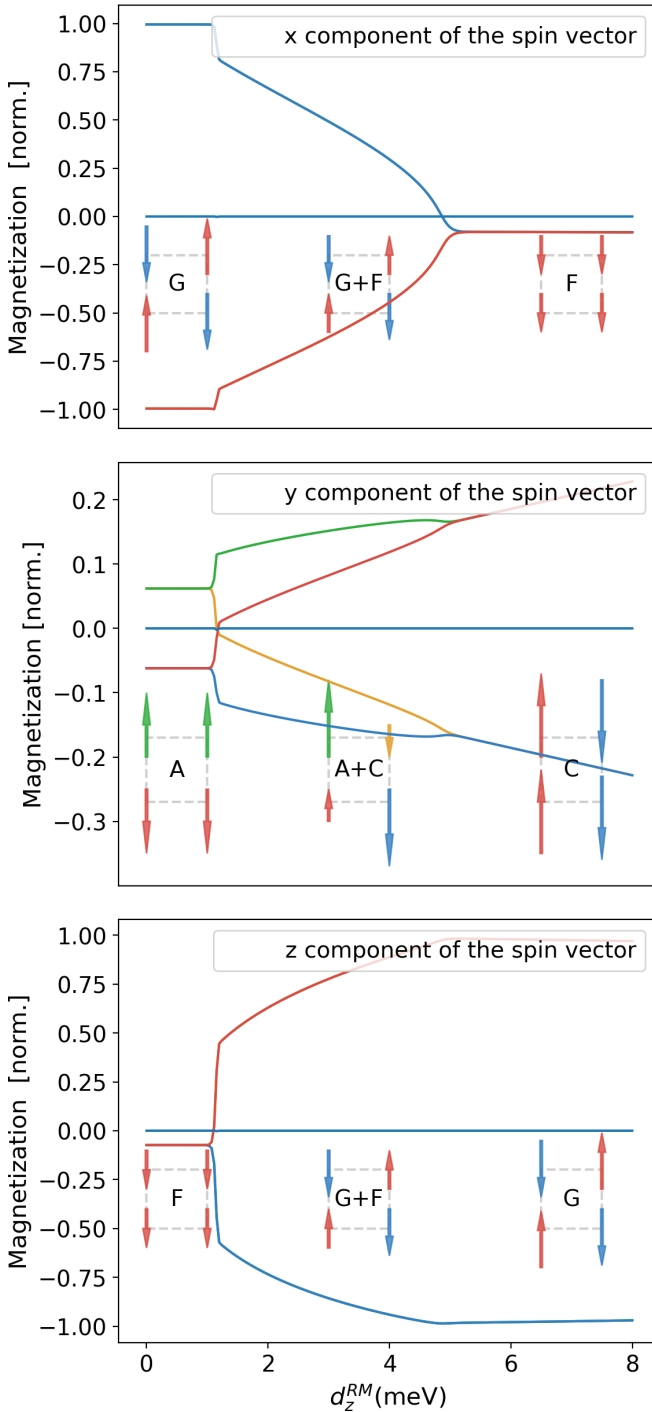
FIG. 9. Decomposition of the total energy from spin dynamics to its components, i.e., energy from superexchange interaction (exch), energy from y componenet of the DMI between M and RM in (d_y^M, d_y^{RM}), and energy from the z component of the DMI between M and RM (d_z^M, d_z^{RM}). The x axis is in the units of meV times the multiplication of the spin amplitudes (see Table II).

FIG. 8. Plot of the evolution of the x, y, and z projections of the local M cation spin components versus the DMI strength between R and M cations. A schematic representation of how the M spins look like is also given for the three main phases Γ_4, Γ_{24}, and Γ_2. The x axis is in the units of meV times the multiplication of the spin amplitudes (see Table II).

2. Origin of the slow Γ_4 to Γ_2 rotation

As we show in the analytical part of our model, there is no interaction between Γ_2 and Γ_4, and we have $\langle \Gamma_2 | H | \Gamma_4 \rangle = 0$. This would mean that the transition should be fast from our model since, without interaction between the two states, there
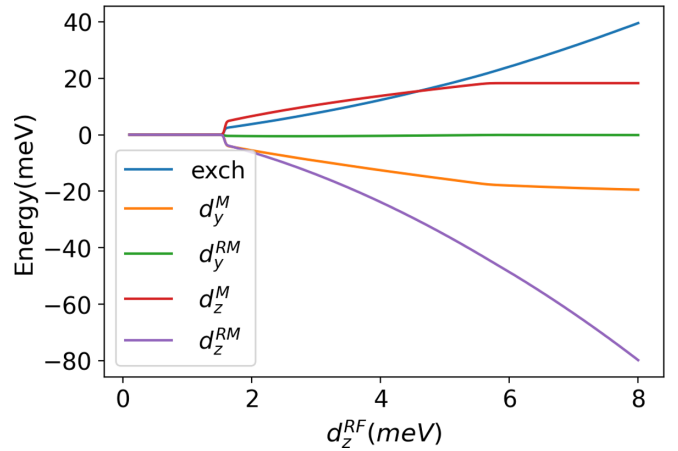
is apparently no reason why their coexistence will reduce the energy, and we should have a sharp transition between them. However, our simulations based on this noninteracting Hamiltonian show that a coexisting region exists where both Γ_2 and Γ_4 are present together.

To figure out what is happening, we plot in Fig. 12(a) the energy change with respect to the d_z^{RM} as decomposed into a pure Γ_4, pure Γ_2, the sum of the energy of Γ_2 and Γ_4, and total energy from our simulations E_{tot}. To understand if there is hidden coupling between Γ_2 and Γ_4 states, we have plotted the sum of energies of Γ_2 and Γ_4 ($\Gamma_2 + \Gamma_4$) and total energy from our simulations E_{tot} and, as we can see, the two energies match exactly which proves that although there is no coupling between the two states, the SR is slow.

In Fig. 12(b) we report the energy decomposition to M sublattice only (M^{Γ_4}, M^{Γ_2}) and interaction between R and M in each state ($RM_{\text{int}}^{\Gamma_4}$, $RM_{\text{int}}^{\Gamma_2}$,). We can see that the M sublattice energy of the Γ_2 state (M^{Γ_2}, blue line) is higher than the energy of the M sublattice in the Γ_4 state (M^{Γ_4}, green line) as expected since the Γ_4 phase is the ground state when only the M sublattice is considered. The two $RM_{\text{int}}^{\Gamma_4}$ (red line) and $RM_{\text{int}}^{\Gamma_2}$ (orange line) interaction terms clearly show that $RM_{\text{int}}^{\Gamma_2}$ lowers the energy of the Γ_2 phase with an amplitude that can compensate the energy difference between M^{Γ_4} and M^{Γ_2}, such that the Γ_2 phase can be lower in energy than the Γ_4 phase. This also proves that the M sublattice alone prefers to stay in the Γ_4 state while the R sublattice pushes the M sublattice to be in the Γ_2 state (the $RM_{\text{int}}^{\Gamma_2}$ energy is stronger and more negative than the $RM_{\text{int}}^{\Gamma_4}$ energy).

In Fig. 13 we show the evolution of the order parameters but decomposed into sublattice contributions (Γ_4-M, Γ_4-R, Γ_2-M, and Γ_2-R). We can observe that in the SR region, when going from Γ_4 to Γ_2 the R spins start to rotate first and they drag the M sublattice afterward (highlighted in the inset). Since the M sublattice prefers to stay in the Γ_4 state while the R-M interaction favors the Γ_2 state, the system ends up in a mixed state even if no Γ_2-Γ_4 interaction is present in
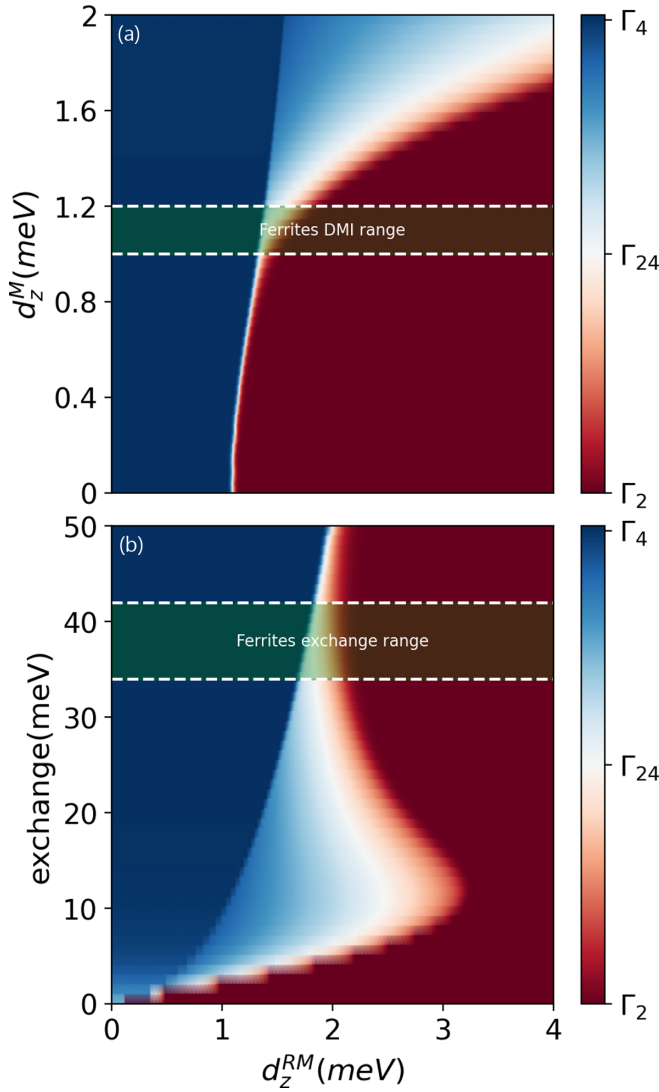
FIG. 10. Phase diagrams for Γ_4 to Γ_2 SR as a function of d_z^{RM} (a) and d_z^M with constant superexchange of 38 meV (corresponding to the ferrites) and between d_z^{RM} and superexchange interaction of the transition metals (b) with constant value of 1.1 meV for d_z^{RM} interaction. The dashed lines with green background showing the DMI (a) and superexchange (b) of iron for the whole range of La family (La to Lu) in RFeO$_3$. The units in x and y axes are in the units of meV times the multiplication of the spin amplitudes (see Table II).

FIG. 11. Phase diagrams for Γ_4 to Γ_2 SR as a function of d_z^{RM} (a) and d_z^M with constant superexchange of 9 meV (corresponding to Cr) and between d_z^{RM} and superexchange interaction of the transition metals (b) with constant value of 0.6 meV for d_z^{RM} interaction. The dashed lines with green background showing the DMI (a) and superexchange (b) of Cr for the whole range of La family (La to Lu) in RCrO$_3$. The units in x and y axes are in the units of meV times the multiplication of the spin amplitudes (see Table II).

the Hamiltonian. To understand this better, note that in this problem we do no really have two competing orders (Γ_2 and Γ_4), but four [$\Gamma_4(M)$, $\Gamma_4(R)$, $\Gamma_2(M)$, and $\Gamma_2(R)$]. As we vary the key Hamiltonian parameter in Fig. 13, the $\Gamma_2(R)$ order becomes favorable over $\Gamma_4(R)$; we thus have a $\Gamma_4 \rightarrow \Gamma_2$ rotation of the R sublattice [accompanied by a relatively tiny $\Gamma_2(M)$ component] that yields a reduction of the energy as compared to a pure Γ_4 state. Eventually, the $\Gamma_2(R)$ order grows and drags the M spins to rotate as well, the final result being a pure Γ_2 state.

3. Effect of SIA on Γ_4 to Γ_2 SR

Although the SIA amplitude on the M site is not very large, we can probe it from our model and have an estimate of its
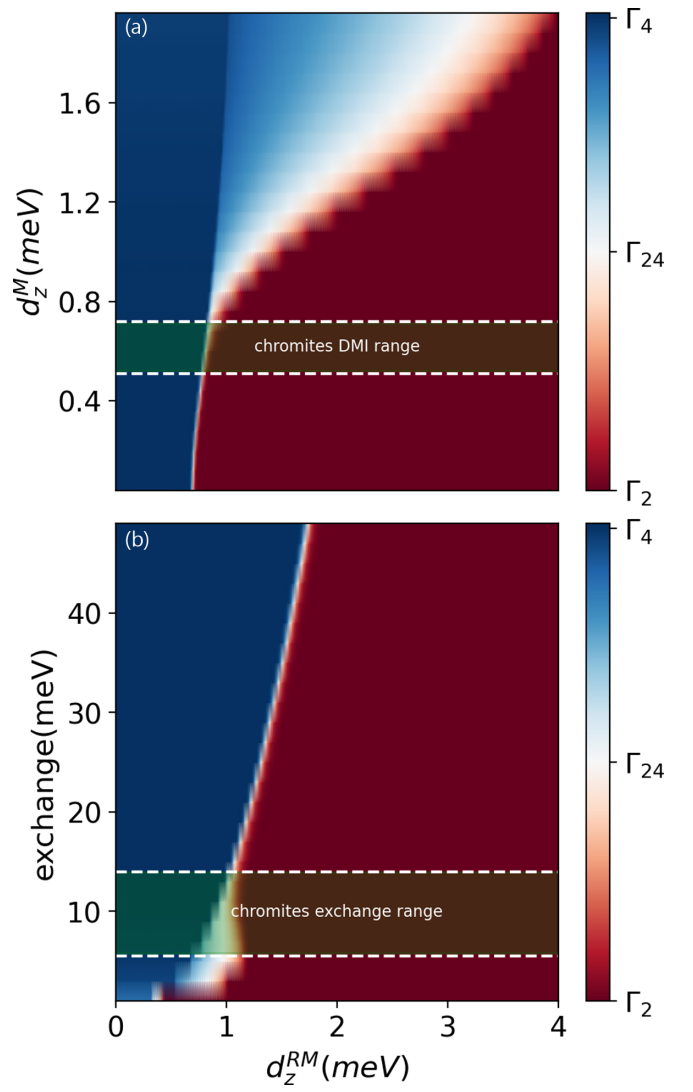
effect on SR. To that end, we report in Fig. 14 the phase diagram of the Γ_4, Γ_2, and Γ_{24} presence with respect to d^{RM} and SIA of M. We can see on this plot that the SIA does not change the Γ_4 to Γ_{24} transition position; in contrast, when the SIA increases, it has the tendency to increase the Γ_{24} SR area at the expense of the Γ_2 state. However, the effect of the SIA is much smaller than the ones of J^M, d^M, or d^{RM}.

4. Summary for the Γ_4 to Γ_2 transition

In summary, in this section we have shown that our model well reproduces the temperature-dependent SR. This behavior shows that the SR is directly linked to the ordering of the rare earth in ferromagnetic order and proves that the mechanism
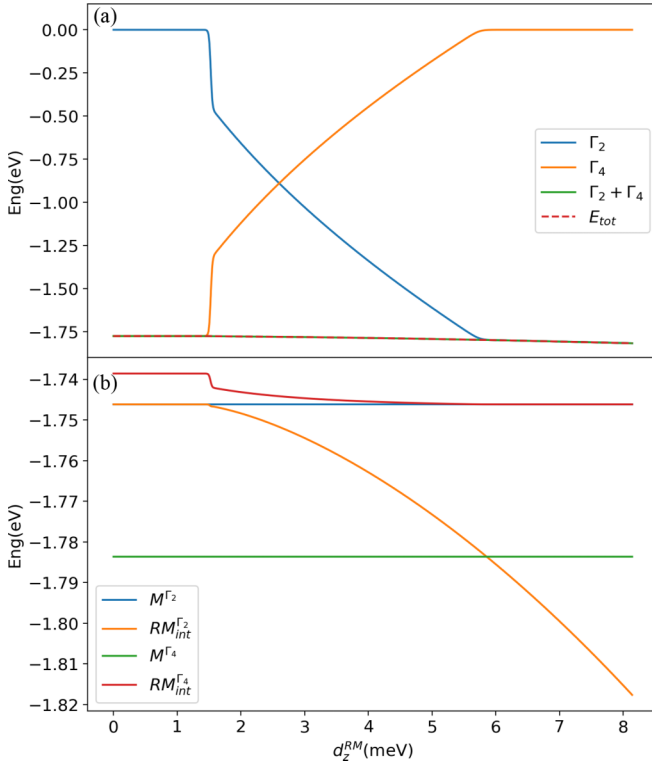
FIG. 12. Decomposition of the energy of the Γ_2 and Γ_4 as a function of d_z^{RM}. (a) Shows the energy of Γ_2 and Γ_4 and $\Gamma_2 + \Gamma_4$ which is the sum of the energies of the two states and E_{tot} which is the total energy from simulations. In (b), the energy of each state is decomposed into its pure M sublattice contributions and the interaction contribution between R and M, the pure R-R interactions being neglected. In (b), the zero-energy reference of M and R interactions is taken to be the one of M^{Γ_2}. We can notice that the RM interacting term is the one that lowers the energy of Γ_2 by becoming larger than the energy difference between pure M^{Γ_4} and M^{Γ_2}. The units in x axis are in the units of meV times the multiplication of the spin amplitudes (see Table II).

behind the SR in $RM O_3$ compounds is not related to the SIA [44], but it is the DMI between R and M that drives this SR.

A study by Vibhakar *et al.* [45] on triple *A*-site columnar-ordered quadruple perovskites has shown that the mechanism behind SR in these structures is the competition between DMI and SIA, which is similar to the mechanism that we found to be at play in $RM O_3$'s SR.

In our simulations, we have also studied how different parameters affect the speed of SR. We can say that the presence of a smooth transition between Γ_4 and Γ_2 phases through a coexisting region Γ_{24} is very subtle and depends on the ratio between J^M, d_z^M, and d_z^{RM} interactions. If d_z^M is zero, a transition between Γ_4 and Γ_2 can exist but only through a first-order abrupt change; the d_z^M interaction is mandatory to have a smooth SR transition.

B. Γ_4 to Γ_1 reorientation

To explain the Γ_4 to Γ_1 SR we need a strong interaction between the R and M sites within the Γ_1 state to allow the M site order to go from its energetically favorable state Γ_4
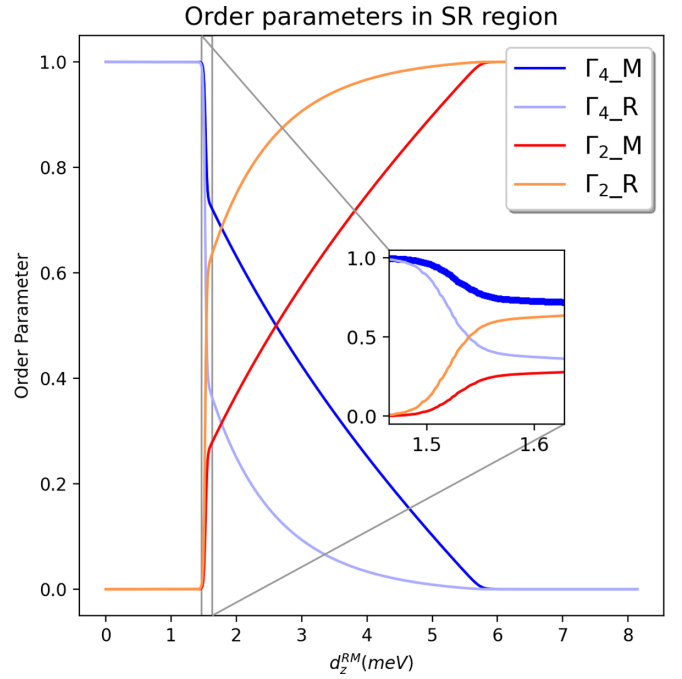

FIG. 13. Order-parameter (Γ_2 with orange color and Γ_4 with blue color) decomposition into M and R sublattices when crossing a SR region (here as a function of d_z^{RM}). The inset shows the area where the SR starts and we can notice the change of order of the R site first that drags the M site order afterward. The units in x axis are in the units of meV times the multiplication of the spin amplitudes (see Table II).

to the less energetically favorable state Γ_1. If not, we would have each sublattice ordering in different direction like what is observed experimentally in TbFeO$_3$ [17]. However, according to our model, the sole interactions between R and M atoms in the Γ_1 state are $-8 N d_x^{RM} C_{R,z} \bar{G}_{M,y}$ and $-8 N d_y^{RM} C_{R,z} A_{M,x}$. The second term is the coupling between $A_{M,x}$ and $C_{R,z}$, which
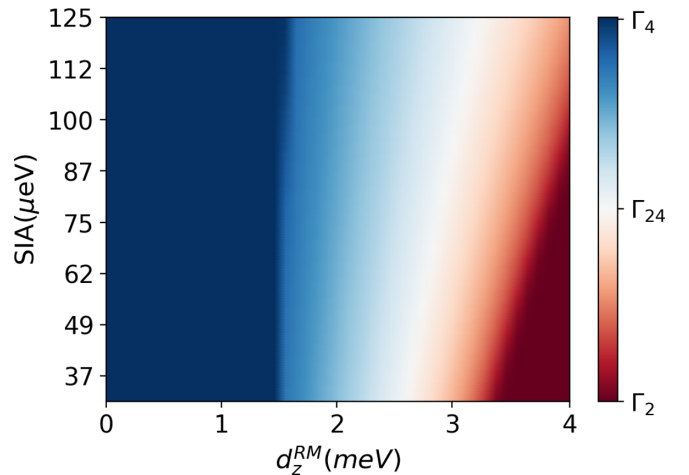

FIG. 14. Effect of SIA on the Γ_4/Γ_2 SR phase diagram. Horizontal axis shows the amplitude of z component of the DMI between R and M sites while the vertical axis shows the amplitude of the SIA of the M site. The units in x axis are in the units of meV times the multiplication of the spin amplitudes (see Table II).

TABLE III. Calculated ASE components from DFT of GdFeO$_3$ and GdCrO$_3$ (units are in meV multiplied by spin amplitude shown in Table II). ε_i are the ASE vector components along $i = x$, y, and z.

	ε_x	ε_y	ε_z
Fe-Fe	−0.015	0.000	0.000
Cr-Cr	0.051	0.000	0.003
Gd-Fe	0.006	−0.016	0.007
Gd-Cr	−0.030	0.010	−0.009

is small since the $A_{M,x}$ canting is very small compared to $\bar{G}_{M,y}$. Hence, the only remaining term which can make this SR possible is $-8Nd_x^{RM}C_{R,z}\bar{G}_{M,y}$. From our DFT calculations and from symmetry analysis (since these parameters are originating from $\bar{a}\bar{a}\bar{c}^+$ oxygen octahedra rotations as discussed in previous section) we know that d_x^{RM} is very small (see Table II) such that it is not possible to explain the Γ_4 to Γ_1 SR using this interaction.

So far we have neglected the anisotropic spin-exchange interactions (ASE) in our model because the effects from these interactions are often negligible with respect to the superexchange or DMI. Now that we have the DMI small too, we will consider the ASE to check whether it can take some importance while the DMI is small. The definitions of DMIs and ASE vector components are as follows:

$$d_x^{ab} = \tfrac{1}{2}\left(J_{yz}^{ab} - J_{zy}^{zb}\right), \tag{17}$$

$$\varepsilon_x^{ab} = \tfrac{1}{2}\left(J_{yz}^{ab} + J_{zy}^{ab}\right), \tag{18}$$

where ε_x^{ab} (d_x^{ab}) represents the ASE (DMI) vector component in the x direction between atom a and atom b and J_{yz} is the superexchange interaction between spins directing in the y direction on atom a and in z direction on atom b (another component, i.e., in y and z directions, can be obtained by cyclic permutation of the xyz directions). We can see that when a component of the DMI vector is small it is probable to have the ASE vector for that component to be bigger depending on the magnitude.

In Table III we show the calculated ASE between Fe and Cr sites. The calculated results show that the x component of the ASE vector is the largest with respect to the y and z components for Fe-Fe and Cr-Cr atom pairs. In Table III we also report the calculated ASE vector for Fe-Gd and Cr-Gd pairs. The biggest component of the ASE vector is in the y direction for Gd-Fe while it is along the x direction for the Gd-Cr case. We note that the ASE interaction in the Hamiltonian takes the same place as the DMI does, i.e., for the Γ_1 state we have

$$-8N\varepsilon_x^{RM}C_{R,z}\bar{G}_{M,y}, \tag{19}$$

$$8N\varepsilon_y^{RM}C_{R,z}A_{M,x}. \tag{20}$$

Considering these ASE interactions, we can say that the Γ_4 to Γ_1 SR can happen through the x component of the ASE (through $-8N\varepsilon_x^{RM}C_{R,z}\bar{G}_{M,y}$ interaction), which will take the place of the DMI when the latter is small. This conclusion is in agreement with Zvezdin [22] who explained the origin of the Γ_4 to Γ_1 SR to originate from ASE.

We will now study this SR by tuning the ε_x^{RM} ASE coupling in our model. In Figs. 15 and 16 we report how the relative Γ_4 and Γ_1 stability evolves with respect to the ε_x^{RM} parameter at 0 K (ground state). In contrast to the Γ_4 to Γ_2 transition we can see that there is no coexisting region between Γ_4 and Γ_1 states, the transition is always abrupt with respect to the ε_x^{RM} amplitude. To confirm this, we also explore in Fig. 15 how the superexchange parameter J^M affects the Γ_4 to Γ_1 SR transition. We can clearly see that whatever value of J^M we considered, the Γ_4 to Γ_1 SR is always abrupt without any coexisting region. We can also remark that J^M favors the Γ_1 state with respect to the Γ_4 state, which can be logically understood by the fact that in the Γ_1 phase all the directions are AFM and, since the torque creating this SR is acting on $G_{M,y}$ (in contrast to Γ_4 to Γ_2 SR where the torque is acting on $C_{M,y}$), the cantings are smaller than in the Γ_4 state. Hence, unlike the Γ_4 to Γ_2 case, the SR involving Γ_1 happens as soon as the system overcomes the energy difference due to ASE and SIA between the two states, making this transition abrupt.
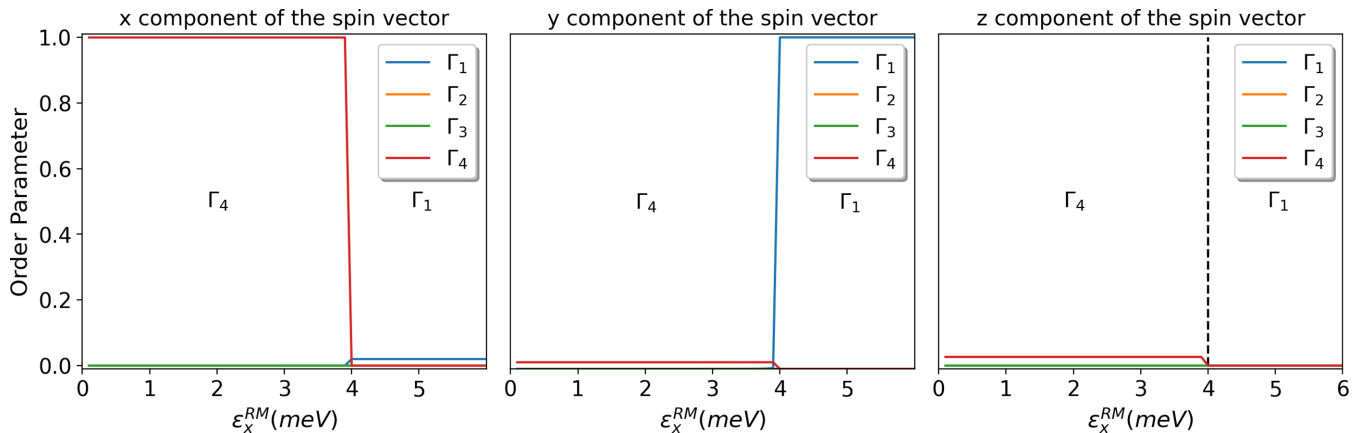

FIG. 15. Magnetic structure for Γ_4 to Γ_1 SR decomposed to different irreducible representations for different components of the spin in x, y, and z directions. The horizontal axis showing the magnitude of ASE in the x direction between R and M and vertical axis showing the order-parameter magnitude normalized. The units in x and y axes are in the units of meV times the multiplication of the spin amplitudes (see Table II).
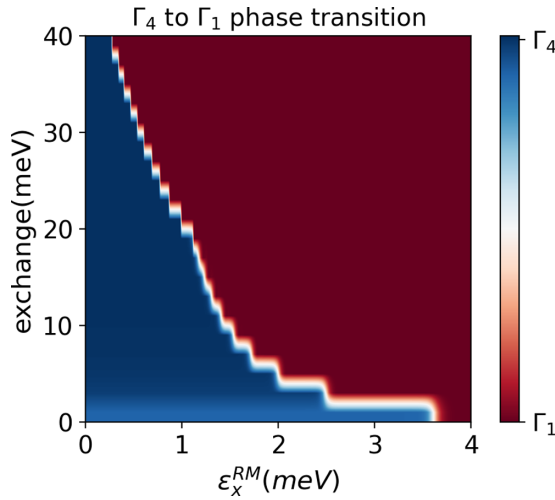
FIG. 16. Phase diagrams of Γ_4 to Γ_1 transition by plotting superexchange on transition-metal sites (J^M) vs the anisotropic exchange ε_x^{RM}. We can see that the SR transition is abrupt for the whole range of superexchange. The units in x and y axes are in the units of meV times the multiplication of the spin amplitudes (see Table II).

We also need to mention that this mechanism explains the Ising-type (strongly collinear) nature of the Γ_1 state [22]. Since the force creating this SR is acting between G-type order of M site and C-type order of R site (i.e., $-8N\varepsilon_x^{RM}C_{R,z}\bar{G}_{M,y}$), the M atoms in Γ_1 state will have a very small canting compared to other states and the spins will mainly order in the G_y type, hence closer to an Ising-type nature.

VI. CONCLUSION

We have studied in this paper the microscopic mechanism behind the SR and MR magnetic behaviors of the RMO_3's through a Heisenberg model where we considered the superexchange interactions and DMI between the transition-metal sites, as well as between the rare-earth (R) and transition-metal sites (M), and we neglected the superexchange and the DMI between the R spins as they are much smaller than the other interaction parameters.

We conclude that there are two interactions polarizing the R atom site, i.e., (i) the superexchange between M sites (through its wFM) and R sites and (ii) the DMI between R and M, which can result into two effects. Indeed, we can have that both interactions polarize the R element parallel to the M wFM canting direction such that there will be no MR but an amplification of the total magnetization of the crystal [see Fig. 1(b), blue curve]. We can also have that both interactions polarize the R element in the opposite direction to the wFM of the M cation such that the total magnetization amplitude can be reduced up to a critical temperature below which its sign

changes [see Fig. 1(b), red curve]. The change of sign appears when the negative R cation magnetization compensates the positive one of the M site (wFM).

Our analysis of the SR transitions has shown that the Γ_4 to Γ_2 transition similarly comes mainly from the DMI interactions between the M and R site but it can be weighted by the superexchange between the M sites. We found that within a relatively wide range of these three interactions this SR transition is smooth and happens through a mixed state where the Γ_4 and the Γ_2 phases coexist even though they do not interact in our Hamiltonian. How broad is the temperature range in which the SR takes place through the Γ_{24} mixed state depends on a subtle ratio between DMI and superexchange interactions between M sites, which can vary depending on the rare-earth and transition-metal cations that are present in the *Pnma* perovskite structure. We also found that the Γ_4 to Γ_1 SR transition depends on even more subtle interactions (anisotropic superexchange that acts as the DMI) but, contrary to the Γ_4 to Γ_2 SR, it never presents a coexisting region, i.e., it always proceeds through an abrupt change.

The model we have presented can help in designing the strength and amplitude of SR and MR in RMO_3 through, e.g., doping, strain, or pressure that would tune the ratio between the key interactions as desired. Our model can also be easily extended by including the interactions between the rare-earth spins to study the complex magnetic phase diagrams below the Néel temperature of the rare-earth sublattice. It can be enlarged too with the anisotropic exchanges (important for the Γ_4 to Γ_1 SR) [22] or with a four-spin interaction term, which has been shown to be important in rare-earth manganites [46]. Because it contains all the key interactions that allow to describe most of the important magnetic properties of RMO_3 compounds, the model can be used to study dynamically magnetic domain walls. Going beyond, the model can be coupled with a lattice model (second principles [47,48]) to have access to a full atom plus spin dynamics for the simulations of, e.g., recent ultrafast laser excitation experiments made on these crystals [49–51].

[1] E. Bousquet and A. Cano, Non-collinear magnetism in multiferroic perovskites, J. Phys.: Condens. Matter **28**, 123001 (2016).

[2] Y. Tokunaga, S. Iguchi, T. Arima, and Y. Tokura, Magnetic-Field-Induced Ferroelectric State In DyFeO$_3$, Phys. Rev. Lett. **101**, 097205 (2008).

[3] Y. Tokunaga, N. Furukawa, H. Sakai, Y. Taguchi, T.-h. Arima, and Y. Tokura, Composite domain walls in a multiferroic perovskite ferrite, Nat. Mater. **8**, 558 (2009).

[4] D. Treves, Studies on orthoferrites at the weizmann institute of science, J. Appl. Phys. **36**, 1033 (1965).

[5] Y. B. Bazaliy, L. T. Tsymbal, G. N. Kakazei, A. I. Izotov, and P. E. Wigen, Spin-reorientation in $ErFeO_3$: Zero-field transitions, three-dimensional phase diagram, and anisotropy of erbium magnetism, Phys. Rev. B **69**, 104429 (2004).

[6] Yamaguchi, Theory of spin reorientation in rare-earth orthochromites and orthoferrites, J. Phys. Chem. Solids **35**, 479 (1974).

[7] H. J. Zhao, J. Iniguez, X. M. Chen, and L. Bellaiche, Origin of the magnetization and compensation temperature in rare-earth orthoferrites and orthochromates, Phys. Rev. B **93**, 014417 (2016).

[8] L. Bellaiche, Z. Gui, and I. Kornev, A simple law governing coupled magnetic orders in perovskites, J. Phys.: Condens. Matter **24**, 312201 (2012).

[9] A. Kimel, A. Kirilyuk, A. Tsvetkov, R. Pisarev, and T. Rasing, Laser-induced ultrafast spin reorientation in the antiferromagnet tmfeo3, Nature (London) **429**, 850 (2004).

[10] J. Kang, Y. Yang, X. Qian, K. Xu, X. Cui, Y. Fang, V. Chandragiri, B. Kang, B. Chen, A. Stroppa, S. Cao, J. Zhang, and W. Ren, Spin-reorientation magnetic transitions in Mn-doped $SmFeO_3$, IUCrJ **4**, 598 (2017).

[11] G. Gorodetsky and L. M. Levinson, Spin re-orientation in sm-feo3, Solid State Commun. **7**, 67 (1969).

[12] V. Skumryev, S. Stoyanov, Y. Zhang, G. Hadjipanayis, D. Givord, and J. Nogues, On beating the superparamagnetic limit with exchange bias, Nature (London) **423**, 850 (2003).

[13] D. Treves, Magnetic studies of some orthoferrites, Phys. Rev. **125**, 1843 (1962).

[14] E. F. Bertaut, *Magnetism*, Vol. 3 (Academic, New York, 1963).

[15] L. T. Tsymbal, Y. B. Bazaliy, V. N. Derkachenko, V. I. Kamenev, G. N. Kakazei, F. J. Palomares, and P. E. Wigen, Magnetic and structural properties of spin-reorientation transitions in orthoferrites, J. Appl. Phys. **101**, 123919 (2007).

[16] E. Constable, D. L. Cortie, J. Horvat, R. A. Lewis, Z. Cheng, G. Deng, S. Cao, S. Yuan, and G. Ma, Complementary terahertz absorption and inelastic neutron study of the dynamic anisotropy contribution to zone-center spin waves in a canted antiferromagnet $NdFeO_3$, Phys. Rev. B **90**, 054413 (2014).

[17] Y. Cao, M. Xiang, W. Zhao, G. Wang, Z. Feng, B. Kang, A. Stroppa, J. Zhang, W. Ren, and S. Cao, Magnetic phase transition and giant anisotropic magnetic entropy change in $TbFeO_3$ single crystal, J. Appl. Phys. **119**, 063904 (2016).

[18] J. R. Shane, Resonance Frequencies Of The Orthoferrites In The Spin Reorientation Region, Phys. Rev. Lett. **20**, 728 (1968).

[19] H. Horner and C. M. Varma, Nature Of Spin-Reorientation Transitions, Phys. Rev. Lett. **20**, 845 (1968).

[20] R. M. White, R. J. Nemanich, and C. Herring, Light scattering from magnetic excitations in orthoferrites, Phys. Rev. B **25**, 1822 (1982).

[21] J. F. Scott, Soft-mode spectroscopy: Experimental studies of structural phase transitions, Rev. Mod. Phys. **46**, 83 (1974).

[22] A. K. Zvezdin and V. M. Matveev, Theory of the magnetic properties of dysprosium orthoferrite, Zh. Eksp. **77**, 1076 (1979) [Sov. J. Exp. Theor. Phys. **50**, 543 (1979)].

[23] A. S. Moskvin and E. V. Sinitsyn, Antisymmetric exchange and four-sublattice model of orthoferrites, Fiz. Tverd. Tela **17**, 2495 (1975) [Sov. Phys. Solid State **17**, 1664 (1976)].

[24] P. W. Anderson, New approach to the theory of superexchange interactions, Phys. Rev. **115**, 2 (1959).

[25] A. S. Moskvin and I. G. Bostrem, Special features of the exchange interactions in orthoferrite-orthochromites, Fiz. Tverd. Tela (Leningrad) **19**, 2616 (1977) [Sov. Phys. Solid State **19**, 1532 (1978)].

[26] P. Hohenberg and W. Kohn, Inhomogeneous electron gas, Phys. Rev. **136**, B864 (1964).

[27] W. Kohn and L. J. Sham, Self-consistent equations including exchange and correlation effects, Phys. Rev. **140**, A1133 (1965).

[28] G. Kresse and J. Furthmüller, Efficiency of ab-initio total energy calculations for metals and semiconductors using a plane-wave basis set, Comput. Mater. Sci. **6**, 15 (1996).

[29] G. Kresse and J. Furthmüller, Efficient iterative schemes for ab initio total-energy calculations using a plane-wave basis set, Phys. Rev. B **54**, 11169 (1996).

[30] P. E. Blochl, Projector augmented-wave method, Phys. Rev. B **50**, 17953 (1994).

[31] J. P. Perdew, A. Ruzsinszky, G. I. Csonka, O. A. Vydrov, G. E. Scuseria, L. A. Constantin, X. Zhou, and K. Burke, Restoring The Density-Gradient Expansion For Exchange In Solids And Surfaces, Phys. Rev. Lett. **100**, 136406 (2008).

[32] A. I. Liechtenstein, V. I. Anisimov, and J. Zaanen, Density-functional theory and strong interactions: orbital ordering in mott-hubbard insulators, Phys. Rev. B **52**, R5467(R) (1995).

[33] X. He, N. Helbig, M. J. Verstraete, and E. Bousquet, TB2J: A python package for computing magnetic interaction parameters, Comput. Phys. Commun. **264**, 107938 (2021).

[34] N. Marzari and D. Vanderbilt, Maximally localized generalized wannier functions for composite energy bands, Phys. Rev. B **56**, 12847 (1997).

[35] A. A. Mostofi, J. R. Yates, G. Pizzi, Y.-S. Lee, I. Souza, D. Vanderbilt, and N. Marzari, An updated version of wannier90: A tool for obtaining maximally-localised wannier functions, Comput. Phys. Commun. **185**, 2309 (2014).

[36] H. Xiang, C. Lee, H.-J. Koo, X. Gong, and M.-H. Whangbo, Magnetic properties and energy-mapping analysis, Dalton Trans. **42**, 823 (2013).

[37] R. F. L. Evans, W. J. Fan, P. Chureemart, T. A. Ostler, M. O. A. Ellis, and R. W. Chantrell, Atomistic spin model simulations of magnetic nanomaterials, J. Phys.: Condens. Matter **26**, 103202 (2014).

[38] See Supplemental Material at http://link.aps.org/supplemental/10.1103/PhysRevB.104.064431 for a mathematical derivation of the energetic expressions used in the main text.

[39] C. Weingart, N. Spaldin, and E. Bousquet, Noncollinear magnetism and single-ion anisotropy in multiferroic perovskites, Phys. Rev. B **86**, 094413 (2012).

[40] N. Shamir, H. Shaked, and S. Shtrikman, Magnetic structure of some rare-earth orthochromites, Phys. Rev. B **24**, 6642 (1981).

[41] Z. Zhou, L. Guo, H. Yang, Q. Liu, and F. Ye, Hydrothermal synthesis and magnetic properties of multiferroic rare-earth orthoferrites, J. Alloys Compd. **583**, 21 (2014).

[42] B. Dash and S. Ravi, Structural, magnetic and electrical properties of fe substituted $GdCrO_3$, Solid State Sci. **83**, 192 (2018).

[43] B. Dash and S. Ravi, Magnetization reversal and exchange bias study in bulk $Gd_{1-x}Y_xCrO_3(x = 0.0$–$1.0)$, J. Magn. Magn. Mater. **461**, 91 (2018).

[44] R. L. White, Review of recent work on the magnetic and spectroscopic properties of the rare-earth orthoferrites, J. Appl. Phys. **40**, 1061 (1969).

[45] A. M. Vibhakar, D. D. Khalyavin, P. Manuel, J. Liu, A. A. Belik, and R. D. Johnson, Spontaneous Rotation Of Ferrimagnetism Driven By Antiferromagnetic Spin Canting, Phys. Rev. Lett. **124**, 127201 (2020).

[46] N. S. Fedorova, C. Ederer, N. A. Spaldin, and A. Scaramucci, Biquadratic and ring exchange interactions in orthorhombic perovskite manganites, Phys. Rev. B **91**, 165122 (2015).

[47] J. C. Wojdel, P. Hermet, M. P. Ljungberg, P. Ghosez, and J. Iniguez, First-principles model potentials for lattice-dynamical studies: general methodology and example of application to ferroic perovskite oxides, J. Phys.: Condens. Matter **25**, 305401 (2013).

[48] P. Garcia-Fernandez, J. C. Wojdel, J. Iniguez, and J. Junquera, Second-principles method for materials simulations including electron and lattice degrees of freedom, Phys. Rev. B **93**, 195137 (2016).

[49] D. Afanasiev, J. R. Hortensius, B. A. Ivanov, A. Sasani, E. Bousquet, Y. M. Blanter, R. V. Mikhaylovskiy, A. V. Kimel, and A. D. Caviglia, Ultrafast control of magnetic interactions via light-driven phonons, Nat. Mater. **20**, 607 (2021).

[50] J. Tang, Y. Ke, W. He, X. Zhang, W. Zhang, N. Li, Y. Zhang, Y. Li, and Z. Cheng, Ultrafast photoinduced multimode antiferromagnetic spin dynamics in exchange-coupled $Fe/RFeO_3$ (r = er or dy) heterostructures, Adv. Mater. **30**, 1706439 (2018).

[51] D. M. Juraschek, M. Fechner, and N. A. Spaldin, Ultrafast Structure Switching Through Nonlinear Phononics, Phys. Rev. Lett. **118**, 054101 (2017).